



### Fiber-reinforced Monolithic Supercapacitor with Interdigitated Interfaces

Journal:	<i>Journal of Materials Chemistry A</i>
Manuscript ID	TA-ART-01-2021-000424.R1
Article Type:	Paper
Date Submitted by the Author:	27-Mar-2021
Complete List of Authors:	<p>Yuan, Fanshu; Nanjing University of Science and Technology, School of Chemical Engineering  Salpekar, Devashish; Rice University  Baburaj, Abhijit; Rice University  Puthirath, Anand; Rice University, Department of Materials Science and NanoEngineering  Hassan, Sakib; Rice University  Robles-Hernandez, Francisco; University of Houston, Mechanical Engineering Technology  Robotjazi, Hossein; Rice University  Saadi, M.A.S.R. ; Rice University  Roy, Soumyabrata; Rice University  Sun, Dongping; Nanjing University of Science and Technology, School of Chemical Engineering  Kotov, Nicholas; University of Michigan, Department of Chemical Engineering  Rahman, Muhammad; Rice University, Materials Science and NanoEngineering  Ajayan, Pulickel; Rice University, Mechanical Engineering and Materials Science</p>

## Fiber-reinforced Monolithic Supercapacitor with Interdigitated Interfaces

Fanshu Yuan,<sup>1,2§</sup> Devashish Salpekar,<sup>1§</sup> Abhijit Baburaj<sup>1§</sup>, Anand B. Puthirath<sup>1</sup>, Sakib Hassan<sup>3</sup>, Francisco C Robles Hernández<sup>4</sup>, Hossein Robatjazi<sup>3</sup>, M.A.S.R. Saadi<sup>1</sup>, Soumyabrata Roy<sup>1</sup>, Dongping Sun<sup>2\*</sup>, Nicholas A. Kotov<sup>5\*</sup>, Muhammad M. Rahman<sup>1\*</sup>, and Pulickel M. Ajayan<sup>1\*</sup>

<sup>1</sup>Department of Materials Science and NanoEngineering, Rice University, TX 77005, USA

<sup>2</sup>Chemicobiology and Functional Materials Institute, Nanjing University of Science and Technology, Nanjing 210094, China

<sup>3</sup>Department of Electrical and Computer Engineering, Rice University, TX 77005, USA

<sup>4</sup>Department of Materials Science and Engineering, University of Houston, TX 77204, USA

<sup>5</sup>Department of Mechanical Engineering, University of Michigan, Ann Arbor, MI, USA

\*Correspondence to: [sundpe301@163.com](mailto:sundpe301@163.com), [kotov@umich.edu](mailto:kotov@umich.edu), [mr64@rice.edu](mailto:mr64@rice.edu), [ajayan@rice.edu](mailto:ajayan@rice.edu)

§ Equal contribution

**ABSTRACT:** Supercapacitors will serve as essential components of distributed energy storage networks and structural power devices in many emerging technologies. Current supercapacitors are engineered, however, using ‘sandwich’ architecture that undermines their physical integrity under stress and at high temperatures due to delamination. It also limits the successful integration of charge storage and load-bearing functions needed to increase the net stored charge. Bridging the requirement of high mechanical and thermal integrity of supercapacitors as structural energy storage elements is still challenging. Addressing these long-standing problems, we demonstrate here a process of developing structural monolithic supercapacitors (MSCs) where all the components are interdigitated by strong nanofibers synthesized from polyaramid fiber (Kevlar® 49). The monolithic design is realized using a one-step stratified assembly of graphene-polyaramid nanofiber (PANF) and boron nitride-PANF nanocomposites acting as electrodes and separator, respectively. MSCs demonstrate an optimum combination of mechanical flexibility and robustness, distributing the stress at interfaces and preventing delamination. Also, combination of thermal stability with fast heat dissipation enables the MSCs to operate at high temperature (~100 °C). Hence, we envisage that MSCs could open prospects for their utilization as structural energy and power system.

**KEYWORDS:** supercapacitors, monolithic, aramid nanofibers, graphene, boron nitride.

## INTRODUCTION

Flexible and lightweight energy storage devices capable of operating at harsh environmental conditions such as mechanical loading or deformation and high temperature are needed for next-generation electronics and electrical equipment.<sup>1</sup> For instance, oil and gas exploration requires underground and underwater robotic device operation at high temperatures.<sup>2,3</sup> Similarly, hybrid electric vehicles (HEVs) use energy storage elements to deliver high power during acceleration and store energy during regenerative braking.<sup>3,4</sup> However, energy storage devices in HEVs that require mechanical stability and proper heat-dissipation need to be placed under-hood for safe operation.<sup>1,3</sup> Likewise, many critical applications such as the high-power electronics industry, defense, and space exploration also require reliable energy storage devices combining high-temperature robustness and rapid heat dissipation.<sup>1,2,4</sup> Furthermore, the future spacecraft, autonomous vehicles, long-haul jets, and delivery drones, including those working in a harsh-environment, are expected to have a distributed power network that can simultaneously serve the purpose of load-bearing and energy storage.<sup>5</sup> A bottleneck in all these applications, however, is the availability of materials that can sustain all these much needed but contrarian properties. Moreover, cost-effective, scalable fabrication of such materials is also vital for their successful realization.

Supercapacitors (SCs) are energy storage devices that can provide such functionalities and offer higher power density and long cycle life compared to both Li-ion batteries and traditional capacitors.<sup>1,6,7</sup> An intensive research effort has been invested in the development of SCs over the last decade; nevertheless, integration of all the functionalities as mentioned above remains a challenge. Ion-conducting membranes commonly used for room temperature SCs, shrink and deteriorate at elevated temperature leading to cathode-anode short circuits.<sup>2</sup> The requirements are

particularly hefty for SCs to be used as load-bearing elements that can markedly increase the net stored charge while decreasing the overall weight. Looking into the path to resolve these problems, one can notice that all SCs reported to date are assembled by hard pressing of electrolyte, separator, and two electrodes,<sup>6</sup> creating large ‘hidden’ stresses at the electrode/separator interfaces compromising the structural integrity and electrochemical performance of the devices and often causing the electrolyte leakage. Monolithic, integrated, and mechanically robust SCs operational under high temperature would be a critical step toward realizing their potential in future electrical and electronics applications.

Here, we report the design and development of a fiber-reinforced monolithic supercapacitor (MSC) using graphene nanosheets (GE), polyaramid nanofibers (PANF), and boron nitride nanosheets (BNNS), taking advantage of vacuum-assisted layering of composite strata. Graphene-polyaramid nanofiber (GE-PANF) nanocomposites<sup>8</sup> act as electrodes, while boron nitride-polyaramid nanofiber (BNNS-PANF) nanocomposites serve as the separator in MSCs. Graphene has high electrical conductivity ( $10^6$  S/m)<sup>9</sup> good chemical & thermal stability, and a large surface area ( $\sim 2675$  m<sup>2</sup>/g).<sup>10-12</sup> On the other hand, PANF, made from *p*-phenylene terephthalamide, is well-known for its mechanical strength (modulus of 103 GPa, tensile strength of 3.8 GPa), flexibility,<sup>13,14</sup> and high-temperature resilience.<sup>15</sup> Although PANF has no electrical conductivity, graphene sheets entangled with PANFs yield a higher degree of flexibility and mechanical reinforcement along with improved porosity and ionic mobility allowing the device to be used as a structural element where the inherent trade-off in electrochemical and mechanical performance can be manipulated. On the other hand, PANFs, along with hexagonal BN provides excellent electrical insulation and thermal management capability<sup>16</sup> while retaining high ionic mobility. Thus, the design combines the electrochemical properties of graphene<sup>17</sup>, thermal management, and

insulating properties of boron nitride, and superior mechanical performances of PANF that interdigitate all the MSC components at critical interfaces, offering remarkably high thermal and mechanical robustness.

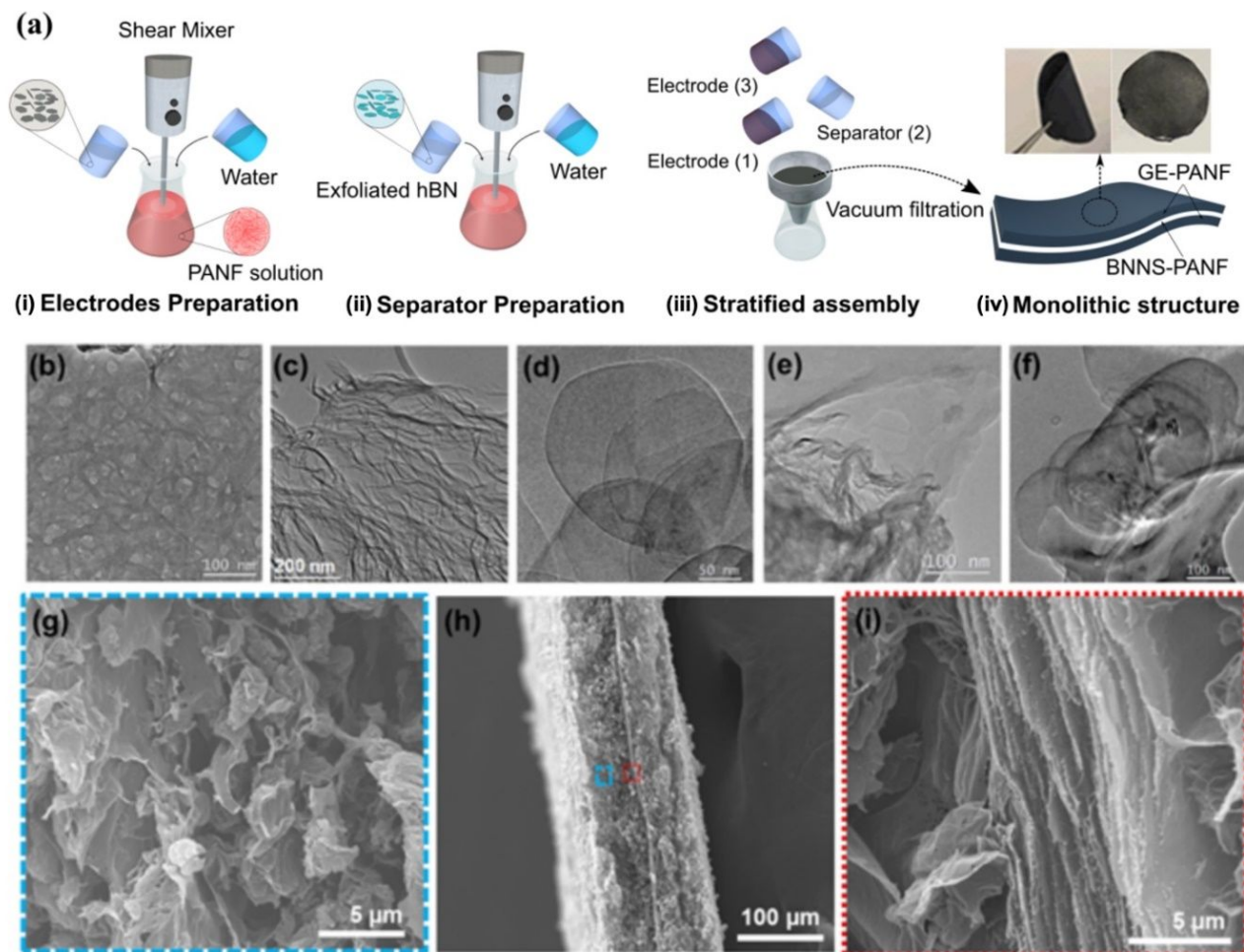


**Figure 1. Fabrication and morphology of MSCs with interdigitated interfaces.**

(a) Schematic illustrations of the fabrication process of MSC: (i) preparation of dispersion for electrode deposition, (ii) preparation of dispersion for deposition of electrolyte/separator layer, (iii) sequential vacuum-assisted deposition of electrodes and separator, (iv) the monolithic structures after drying, in an unfolded and folded state. TEM images of the (b) PANF, (c) exfoliated graphene (GE), (d) BN nanosheets (BNNS), (e) GE-PANF composite, and (f) BNNS-PANF composite. Cross-sectional SEM images of (g) GE-PANF composite in the monolithic structures, (h) complete monolithic structures showing the thickness of MSC, (i) BNNS-PANF composite in the monolithic structures.

## RESULTS AND DISCUSSION

### Fabrication and Morphology of Monolithic Supercapacitor

The monolithic devices were fabricated following the process depicted in **Figure 1a** (see Experimental Section for more details). In a typical experiment, the 1<sup>st</sup> electrode is fabricated by mixing the desired amount of PANF dispersion in Dimethyl sulfoxide (DMSO) with GE-DMSO dispersion, followed by the addition of water for re-protonation of PANF. The resulting GE-PANF dispersion was deposited on a nylon membrane by filtration. Then the separator layer was fabricated on top of the 1<sup>st</sup> electrode layer by filtrating similarly-prepared BNNS-PANF dispersion. Finally, the 2<sup>nd</sup> electrode layer, with the same composition as the 1<sup>st</sup> one, was deposited on top of the BNNS-PANF stratum. The final free-standing monolithic structure was obtained by rinsing the as-prepared monolith with DI water and then drying at 90 °C for 48h in a vacuum oven. The free-standing, black-colored monolithic structure had a smooth surface, high flexibility, and foldability, reflecting the structural integrity of the film (**Figure 1a**).

The design of MSC is based on nanocomposite sheets that were developed by integrating one-dimensional (1D) PANF and two-dimensional (2D) GE and BNNS. PANF serves as the principal building block preventing delamination at interfaces, while GE sheets act as structural electrodes, and BNNS provides the electrical insulation between electrodes while enhancing the thermal conductivity of the stratified nanocomposite. To analyze the structural features of PANF, GE, BNNS, BNNS-PANF, and GE-PANF in nanoscale dimensions, we conducted transmission electron microscopy (TEM) studies. PANF showed a mostly fibrous network structure (**Figure 1b**). Additionally, there were crystalline areas observed in PANF with *d*-spacings of 0.33 and 0.24 nm (**Figure S1a**, Supporting Information), corresponding to the (110) and (004) planes, respectively, that matches with the parent para-aramid fibers.<sup>18</sup> The nanofibers had diameters

ranging from 15-30 nm, and the length of these fibers is in the range of 10-20  $\mu\text{m}$ .<sup>16</sup> **Figure 1c** shows exfoliated graphene in DMSO. Moreover, imaging of the precipitations from GE-PANF clearly shows the characteristic *d*-spacing of graphene (0.33 nm) (**Figure S1b**, Supporting Information),<sup>19</sup> which demonstrates that the processing did not affect the structural integrity of graphene. It is noted that PANF and graphene have the same *d*-spacing, although GE is layered and PANF has a well-defined semi-crystalline structure. BNNS was obtained through the liquid phase exfoliation of hexagonal boron nitride powders in DMSO (**Figure 1d**). The lateral sizes of BNNS were in the range of 50-300 nm with a thickness of 5-15 nm (**Figure 1d**).<sup>16</sup> TEM results obtained for BNNS-PANF nanocomposite do not show any change in the integrity of BNNS (**Figure S1c**, Supporting Information). Besides, both the GE-PANF and BNNS-PANF (**Figures 1e and 1f**) show that PANF network wraps the BN and GE nanosheets homogeneously, which ensures the strong interactions between the nanoscale components.

A cross-sectional SEM image of the MSCs revealed the well-stacked structures and thickness of the integrated film (**Figure 1h**) where the BNNS-PANF insulating layer is sandwiched between two GE-PANF electrode layers (**Figure 1g**). The SEM image of the BNNS-PANF stratum shows a lamellar stacked structure with PANF interconnecting each BN nanoplatelets (**Figure 1i and S2a**, Supporting Information). Similarly, close observation of GE/PANF nanocomposite showed that GE is intercalated between homogeneously distributed and entangled PANF network (**Figure S2b**, Supporting Information). It is noted that the flexibility of the monolithic architecture of MSC is possible due to the long-range PANF entanglement (**Figure S2**, Supporting Information) that is reminiscent of many nanofibrous architectures found in biology.<sup>20-22</sup> The robustness comes from the effective stress transfer due to the high aspect ratio of the nanofibers and strong non-covalent interactions such as van der Waals forces and hydrogen bonds within the structural components

arising from abundant polar functional groups such as amide (-CONH-) groups.<sup>23</sup> The final thickness of the monolithic structure, as determined by SEM, was found to be around 150-180  $\mu\text{m}$ .

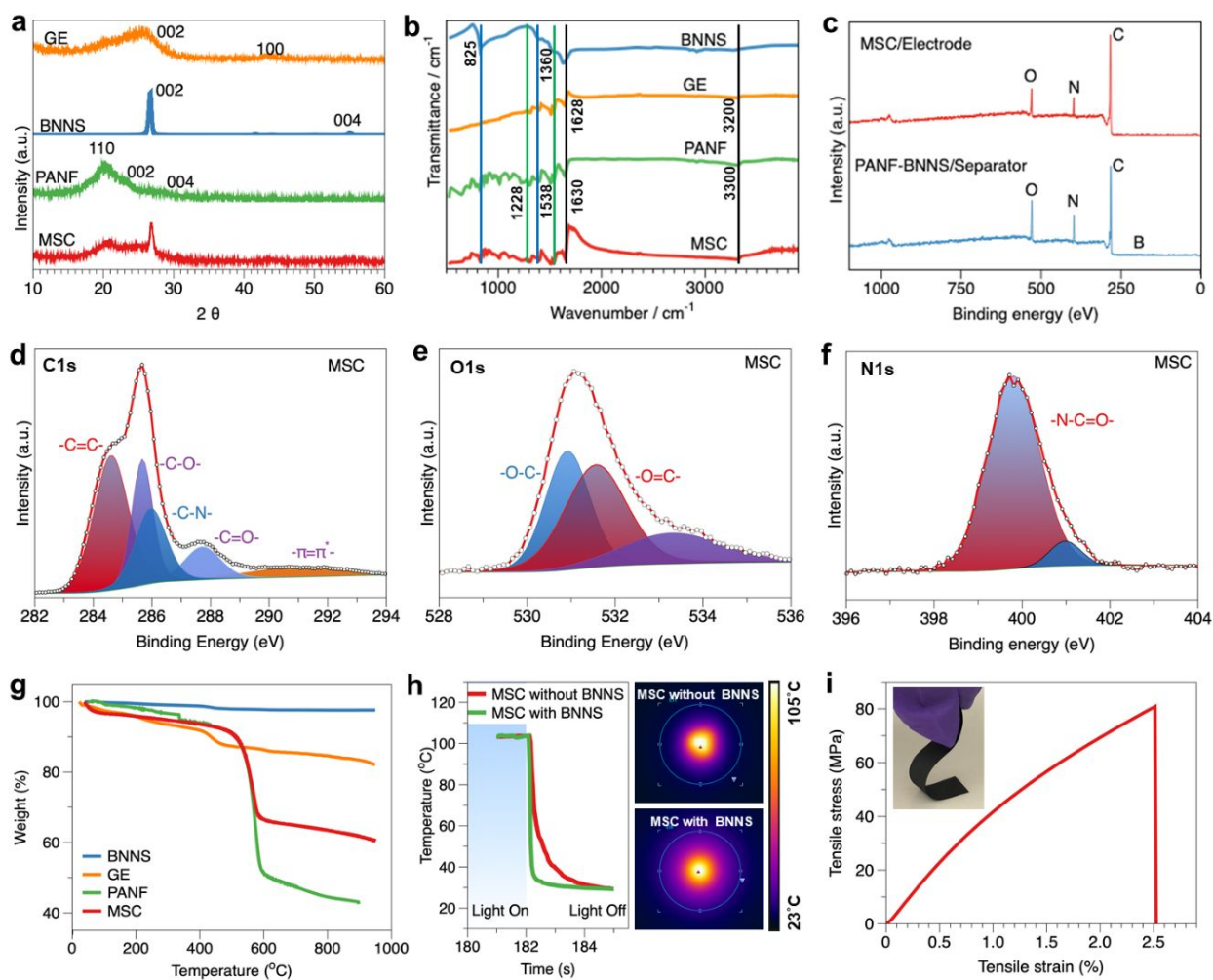


**Figure 2. Structure and properties of MSCs with interdigitated interfaces.**

(a) X-ray diffraction pattern of BNNS, GE, PANF, and MSC, (b) FTIR spectra of BNNS, GE, PANF, and MSC, (c) XPS survey scan of MSC/electrodes and PANF-BNNS or separator, (d) XPS C1s spectra, (e) O1s spectra, (f) N1s spectra of MSC/electrodes and (g) Thermogravimetric analysis of PANF, GE, BNNS, and MSC sheet showing the thermal stability of MSC, (h) Steady-state temperature monitoring with spatial temperature mapping of the MSC surface without- and with BNNS sheet during illumination (450 nm) in air. (i) Typical tensile stress-strain plots of MSC sheet showing the high strength and stiffness, while the inset demonstrates the flexibility of the sheet.

## Structural Features of Monolithic Supercapacitor

Next, the integration of the monolithic structure is confirmed and analyzed by X-ray diffraction (XRD), Fourier-transform infrared spectroscopy (FTIR), and x-ray photoelectron spectroscopy (XPS) studies. XRD patterns of the BNNS, GE, PANF, and the MSC stack are shown in **Figure 2a**. The BNNS exhibited peaks at  $26.7^\circ$  and  $54.9^\circ$  corresponding to the diffraction of the (002) and (004) planes with no peak shifting or broadening compared to that of pure BN powder. This indicates minimal damage to the in-plane structure of BNNS during the exfoliation process.<sup>24</sup> Similarly, two peaks at  $26.5^\circ$  and  $43.1^\circ$  are assigned to the characteristic (002) and (100) plane reflections of graphite from the restacked GE sheet, respectively.<sup>25</sup> Pure PANF sheet exhibits broad peaks in the range of  $20^\circ$ - $30^\circ$ , corresponding to the (110), (200), and (004) planes similar to that of macro-scale aramid fibers, which indicate PANF maintained the crystallinity in the nanoscale domain.<sup>26</sup> XRD patterns of the MSC confirmed all the characteristic peaks of PANF, BNNS, and GE.

Interdigitation of interfaces in our MSCs was also studied by FTIR spectroscopy (**Figure 2b**). The spectra for pure PANF show a band at  $3300\text{ cm}^{-1}$  related to the N-H bending and stretching vibration. The other main characteristic peaks were assigned as  $1630\text{ cm}^{-1}$  (C=C stretch and secondary amide),  $1538\text{ cm}^{-1}$  (N-H bend), and  $1228\text{ cm}^{-1}$  (C-N amine stretching), corresponding to the distribution of atoms in the PANF framework.<sup>27</sup> For BNNS, two major peaks were observed at  $1360\text{ cm}^{-1}$  and  $825\text{ cm}^{-1}$ , corresponding to B-N transverse optical mode and B-N-B out-of-plane bending vibrations, respectively.<sup>28</sup> GE shows major characteristic peaks at  $3060\text{ cm}^{-1}$  (C-H stretching in alkene),  $1973\text{ cm}^{-1}$  (C-H bending in alkene), and  $1628\text{ cm}^{-1}$  (C=C stretching).<sup>29</sup> For integrated monolithic structures, the dominant peaks are labeled in the figure, matching perfectly for GE, BNNS, and PANF with no peak shifting, which indicates no covalent interaction among

the nanomaterials. However, the changes in the intensity of the peaks suggest the formation of hydrogen bonding or electrostatic interactions at the interfaces among the materials.<sup>30</sup>

We performed X-ray photoelectron spectroscopy (XPS) to verify the elemental composition and confirm the nature of intermolecular interactions between the constituent elements in the electrode/MSM and separator surface (**Figure 2c**). From the XPS spectra of electrodes and MSCs, it is observed that the C1s spectra are deconvoluted into five different bands: the first one at ~284.51 eV corresponds to sp<sup>2</sup>-hybridized graphitic carbon from graphene, and the second one (~285.65 eV) corresponds to the carbon bonded to nitrogen in the aramid macromolecules. Surprisingly, a small peak was observed at ~286 eV, which indicated the presence of oxygen functional groups due to partial oxidation of carbon (**Figure 2d**).<sup>31</sup> The fourth peak ~288 eV corresponds to the -C=O bonding in the aramid structure, and finally, the  $\pi$ - $\pi^*$  between the graphene layers is observed at 291.2 eV. The deconvoluted O1s spectra (**Figure 2e**) of MSCs show three major peaks at 531.2, 532.5, and 533.5 eV corresponding to the oxygen in -O-C-, O=C-, and hydrogen bonding in the PANF, respectively. The deconvoluted N1s spectra (**Figure 2f**) shows a major band at 399.1 eV corresponding to the nitrogen in -N-(C=O)- from the PANF in the electrodes.<sup>32</sup> The atomic percentage of the C, O, and N in the electrodes were 84.0%, 9.0%, and 7.0%, respectively. On the other hand, the C1s spectra in the ion-conducting PANF-BNNS composite were deconvoluted into three different bands. A dominant peak at 284.5 eV corresponds to the sp<sup>2</sup> carbon atoms within the aromatic ring. The peak at 285.2 eV corresponds to the carbon atoms attached to the C=O group, while the smallest peak at 287.7 eV stands for the carbon on the C=O functional group. The B1s spectrum has a peak at 190.4 eV, which matches the energy of the B-N bond. N1s spectra can be curve fitted into two peaks: 398.0 eV (BN) and 399.9 eV (N-(C=O)-

). According to the analysis, the PANF-BNNS stratum contains 73.0% carbon, 14.0% oxygen, 12% nitrogen, and 1.0% boron (**Figure S3**, Supporting Information).

### **Thermal and Mechanical Stability of Monolithic Supercapacitor**

Before electrochemical studies, we analyzed the thermal stability of the monolithic structures. For thermoset polymers, the glass transition temperature ( $T_g$ ) is the maximum operating temperature, and high  $T_g$  is desirable for practical applications.  $T_g$  of MSC was determined to be around 280 °C from differential scanning calorimetry (DSC) heating curves (Figure S5, Supporting Information), which are significantly higher compared to many conventional commercial polymers utilized in modern electronics such as polyethylene terephthalate ( $T_g \sim 75^\circ\text{C}$ ), polyphenylene sulfide ( $T_g \sim 120^\circ\text{C}$ ), and polycarbonate ( $T_g \sim 150^\circ\text{C}$ ). Additionally, MSCs showed minimal thermal degradation below 510°C as determined by weight losses using thermogravimetric analysis (TGA) (**Figure 2g**). This could be achieved due to the high thermal stability of the individual constituents. BNNS showed no significant loss in weight upon heating, whereas GE retains around 84% of its initial weight even after heating to 900 °C. MSC retains around 62% of the initial weight, where the weight loss can be directly associated with the PANF decomposition at 510 °C.<sup>33</sup> Any weight loss before 200 °C is primarily attributed to the loss of water due to evaporation rather than material degradation.

The steady-state heating of the MSCs with (modified) and without BNNS (unmodified) in the electrolyte layer identified the role of BNNS in the overall heat transport. We performed photothermal heating measurements under a continuous wave, CW (532 nm,  $\sim 3$  mm spot size) laser illumination in air. Steady-state surface temperatures under illumination and after the light turned off were monitored using a thermography infrared (IR) camera (FLIR A165) at spatial and temporal resolutions of  $\sim 100$  microns and 25 frames/second, respectively (**Figure 2h**). A nominal

surface temperature of 105 °C was established on each sample by using an illumination power of 20 mW and 40 mW for the unmodified and modified MSC, respectively. The necessity for a higher illumination power on the modified MSC to achieve a similar surface temperature suggests an increase in the thermal conductivity of the MSC on BNNS incorporation. The larger thermal conductivity of the BNNS-modified sample resulted in a substantially faster heat dissipation rate (**Figure 2h**). Once the irradiation was turned off, the modified sample instantaneously cooled down to near the ambient temperature with the first-order heat dissipation kinetics (**Figure S6, S7**, Supporting Information). In contrast, the unmodified sample showed a much slower heat dissipation rate that follows fifth-order decay kinetics (**Figure S6**, Supporting Information). Consistently, the spatial surface temperature distributions show a more localized light-induced heating for the unmodified sample due to a lower thermal conductivity compared to the BNNS-MSC (**Figure 2h**). With the excellent thermal properties, next, we investigated the mechanical properties of the MSC. The integrated structure is foldable and flexible (**Figure 1a and 2i**). PANF sheet showed a tensile strength of  $88.0 \pm 12.0$  MPa and Young's modulus of  $6.0 \pm 1.0$  GPa. The addition of graphene and BNNS in the monolithic structures did not affect the modulus and strength significantly. The flexibility of this free-standing nanocomposite sheet is mainly due to the long-range PANF entanglement. The tensile strength was decreased slightly to  $70 \pm 30$  MPa, while the modulus was calculated to be around  $5.0 \pm 0.8$  GPa.

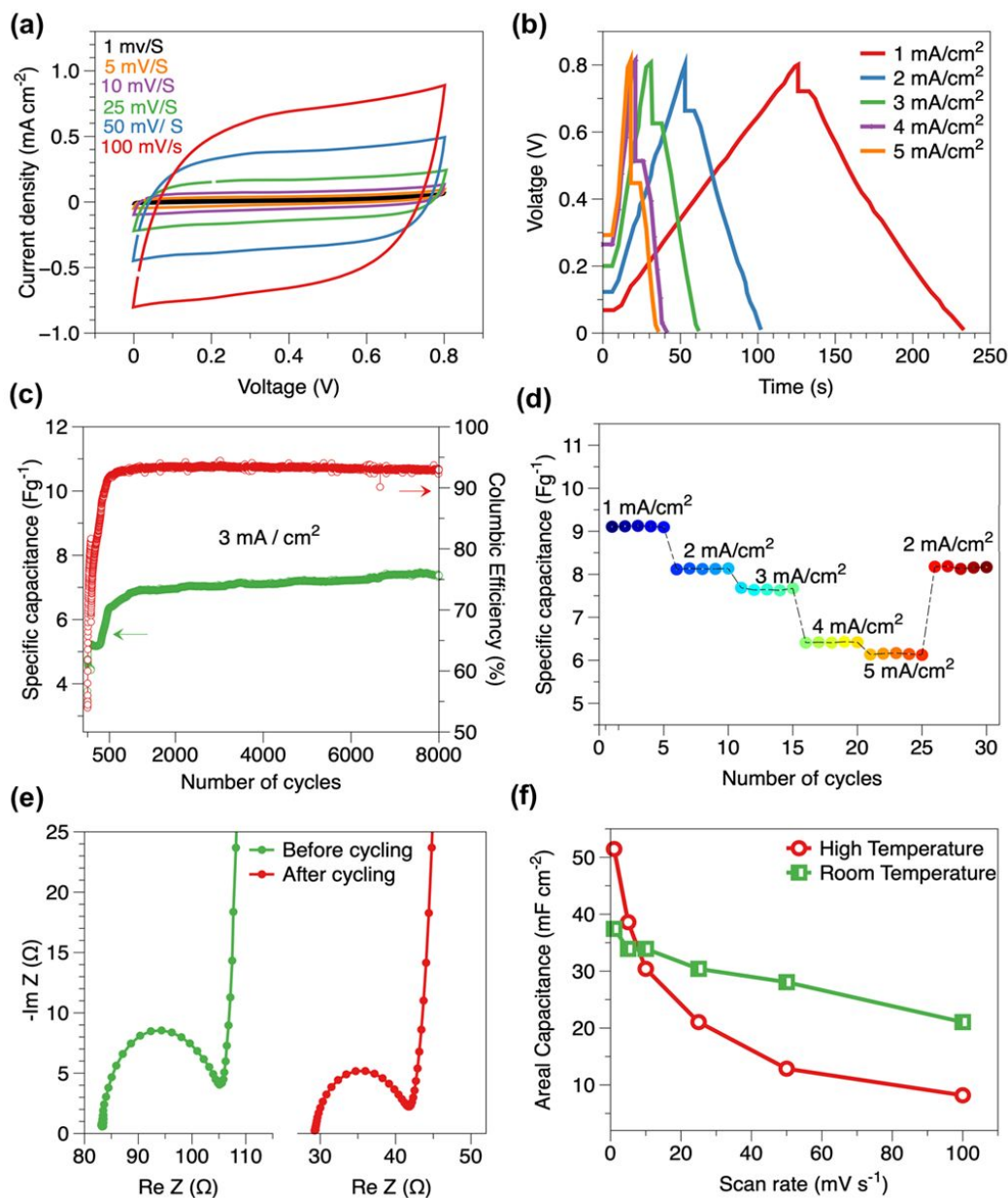


**Figure 3. Electrochemical characterization of MSCs with interdigitated interfaces.**

(a) Cyclic voltammety of MSCs at different voltage sweep rates. (b) Galvano-static charge-discharge curves of the MSC at different current densities. (c) Cycling stability of the MSCs at  $3 \text{ mA/cm}^2$  over 8000 cycles. The slight increase in capacitance observed here is ascribed to the better wetting of the electrodes with the electrolyte during the cycling and also some self-activation processes.<sup>34</sup> (d) Discharge specific capacitance of the MSC at different current densities. (e) Impedance behavior of the MSCs at room temperature before and after cycling. (f) Areal capacitance dependence on potential sweep rate at room temperature and a temperature of  $100^\circ\text{C}$ .

### Electrochemical Performance of the Monolithic Supercapacitor

The electrochemical performance of the MSCs was studied by cyclic voltammetry (CV), and galvanostatic charge-discharge (GCD) tests both at room and high temperatures using CR2032 coin cell configuration. Prior to the assembly, the MSCs were soaked in an electrolyte solution of 6M KOH for 24 h. The soaked MSCs were sandwiched between two stainless-steel spacers to avoid contact loss in the coin-cell. The CV curve of the MSCs demonstrates ideal Electric Double Layer Capacitor (EDLC) behavior, *i.e.*, rectangular, which was retained even at a high scan rate of 100 mVs<sup>-1</sup> (**Figure 3a**). The concept of specific capacitance has been adopted as an important parameter in evaluating the MSC electrode materials. The CV studies were performed in a voltage window of 0-0.8V, and the scan rate was varied between 1 mV/s to 100 mV/s (**Figure 3a**). The specific capacitances observed for 1, 5, 10, 25, 50 and 100 mV/s are 27, 21, 20, 19.5, 19, and 18 F/g respectively. It is worth noting that, unlike measuring the capacitance via a three-electrode cell that gives more of a material-specific property, the capacitance values obtained here are derived out of two-electrode configuration supercapacitor cells and can be considered as the actual device level capacitances.<sup>35</sup> Therefore, due to inherent cell configuration differences, our device shows comparatively lower capacitance than most commonly reported three-electrode configuration displaying higher capacitance value.<sup>36</sup> While converting to areal capacitance (Equation S1-S3), a maximum capacitance of 37 mF/cm<sup>2</sup> was observed at a 1 mV/s scan rate. The quasi-rectangular CV curve indicates capacitive charge storage by an electrical double-layer mechanism without any sign of pseudocapacitive behavior.<sup>37</sup> This mechanism facilitates the retention of capacitance values, even at higher current discharge rates. Comparatively, moderate capacitance observed here could be due to the masking of the active surface area of the electrodes while engineering the flexible device architecture *via* sequential layering of composite strata. This can be tackled by

replacing a few layers of graphene with highly porous and conducting carbon materials. After conducting the CV studies, GCD cycling was conducted to determine the performance of the device over time at different current densities. The discharge profiles of the capacitor are depicted in **Figure 3b**, and the devices show an IR loss of the order of 60 mV, 120 mV, 180 mV, 250 mV, and 300 mV in the discharge regime for 1 mA/cm<sup>2</sup>, 2 mA/cm<sup>2</sup>, 3 mA/cm<sup>2</sup>, 4 mA/cm<sup>2</sup>, and 5 mA/cm<sup>2</sup>, respectively. Such cumulative IR loss is expected as the equivalent series resistance (ESR) value observed is close to 100  $\Omega$  for our devices and is described in the later part of the manuscript. In the CV, such voltage drop will not be observed due to the voltage sweep; however, it will be explicit in the charge-discharge curves where voltage variation is measured by supplying constant currents. After 8000 charge-discharge cycles, no capacitance reduction is observed, as shown in **Figure 3c**, and the MSC retained 93% of Coulombic efficiency (red line). Fluctuation in the capacitance value is observed during the very initial cycles, which is expected due to the cell formation and stabilization process under an applied voltage. Unlike to what is seen in the CVs, due to high ESR the rate-dependent discharge curves (**Figure 3d**) show a moderate fall in the specific capacitance (30%) while sweeping from 1 mA/cm<sup>2</sup> to 5 mA/cm<sup>2</sup>. Moreover, the superior cyclic stability can be attributed to the hydrogen bonding interactions between PANF and GE or BNNS facilitating large volumetric expansion and shrinkage during the charge and discharge process.<sup>38,39</sup> On the other hand, the Electrochemical Impedance Spectroscopy (EIS) data expressed as Nyquist plots (**Figure 3e**) shows the effects of the cycling in the supercapacitor system consisting of the electrode/electrolyte/current collector. The small semicircle shows an electrochemical series resistance (ESR) value of 83  $\Omega$  before cycling, which decreases to 30  $\Omega$  after cycling due to enhanced wetting of the integrated insulator module during cycling, further improving the capacitance.<sup>40</sup> We further studied the electrochemical properties of the flexible MSC

device under bent conditions and more discussion with the results are depicted in supplementary information section (**Figure S8 and S9**).

Finally, we investigated the electrochemical performance of MSCs at a high temperature. For high-temperature operation, we used ionic liquid (1-ethyl-3-methylimidazolium bis (trifluoromethylsulfonyl) imide (EMI-TFSI)) as the electrolyte instead of KOH. Due to the high thermal stability of all the materials used, the MSC configuration exhibited stable performance at elevated temperatures (100°C). The CV results of MSCs at high temperatures show a rectangular IV profile (**Figure S10**, Supporting Information). At a low scan rate, the areal capacitance was found to be ~51 mF/cm<sup>2</sup>, while the capacitance decreases at a high scan rate. It is interesting to note that the capacitance at high temperature is similar to the room temperature values at low scan rates. However, at higher scan rates, the high-temperature operation has shown lower capacitance than the room temperature values (**Figure 3f**). We ascribe this to different mass transport kinetics in the ionic and aqueous electrolytes at different scan rates.<sup>41</sup> The ionic radii of OH<sup>-</sup> is 0.11 nm, while TFSI<sup>-</sup> possesses a comparatively high radius of 0.79 nm, and therefore, higher mass.<sup>42</sup> Moreover, at high-temperature, the conductivity of the ionic liquid is inferior compared to aqueous electrolytes. The kinetics of mass transport at high scan rates happen to be low for ions in ionic liquid and high for small ions in aqueous electrolytes.<sup>43</sup> However, the successful and stable high-temperature operation, even with moderate capacitance value compared to other studies, makes this device promising for many harsh-environment applications.

## CONCLUSIONS

In summary, stratified device architecture with all interfaces interpenetrated by the ultra-strong nanofibers enabled the realization of previously unknown monolithic charge storage devices. The hierarchical stacking of entangled nanofiber-nanosheet composites in the device provides a unique

combination of excellent mechanical and thermal stability along with moderate electrochemical performance. Better thermal management capability due to BNNS nanocomposites and delamination prevention at the electrode/electrolyte interfaces allows stable operation of MSCs at high temperatures. Although the electrochemical performance requires further optimization by trading off among mechanical, thermal, and capacitance properties, the reported approach of making MSCs device will open new avenues for developing next-generation mechanically stable and high-temperature energy storage devices.

## **EXPERIMENTAL SECTION**

### **Materials**

Hexagonal boron nitride (h-BN) powder (Sigma-Aldrich, average diameter: 1  $\mu\text{m}$ ), Polyaramid fiber (Kevlar 49<sup>®</sup>), analytical grade potassium hydroxide (KOH), and dimethyl sulfoxide (DMSO) were purchased from Sigma-Aldrich. Graphene powder was obtained from Angstrom Materials. All the materials were used as obtained without any purification.

### **Preparation of poly-aramid nanofiber (PANF) dispersions**

The PANF dispersions were prepared from aramid fiber by a controlled deprotonation and dissolution process. 2 mg/ml of PANF dispersion was prepared by magnetically stirring 1 g of Kevlar 49<sup>®</sup> fiber in DMSO for 7 days in the presence of 1.5 g KOH.

### **Preparation of GE-PANF dispersions**

GE-DMSO dispersion was prepared *via* exfoliating and dispersing graphene in DMSO for 1h using a tip-type sonicator. The desired amount of PANF-DMSO dispersion (2 mg/ml) was slowly added into GE-DMSO dispersion (1 mg/ml) and vigorously stirred for 1 h. Then, DI water was added to the mixture that resulted in hydrogel formation between PANF and GE. The hydrogel

mixture was stirred vigorously for 15 min at 9000 rpm by a high-speed homogenizer (IKA T-25 digital Ultra-Turrax) to ensure a homogeneous mixture.

### **Preparation of BNNS-PANF dispersions**

BNNS-DMSO dispersions were prepared *via* exfoliating and sonicating h-BN powder in DMSO for 6 h. The resulting dispersions were centrifuged at 3000 rpm for 15 min to remove non-exfoliated h-BN. Then, the supernatant was collected and sonicated for another 15 min using a tip-type sonicator. Finally, the obtained BNNS-DMSO suspension was concentrated to 0.5 mg/ml. To prepare BNNS-PANF solution (5 wt.% BN), the process is the same as the GE-PANF solution besides using BNNS-DMSO suspension instead of GE-DMSO suspension.

### **Assembly of monolithic supercapacitor**

The three-layer electrodes were fabricated using an alternating vacuum-assisted filtration method. 20 mL of GE-PANF dispersion was filtered on a nylon filter membrane (47 mm diameter with a pore size of 0.22  $\mu\text{m}$ ) by vacuum filtration assembly. Then, 20 mL of the BNNS-PANF solution was filtered on the top of the GE layer. Finally, 20 mL of GE-PANF dispersion was alternately filtered on the top of the BN layer. The obtained nanocomposite films were then washed with an ample amount of DI water to remove any contaminants and kept firmly between two glass slides in a vacuum oven at 90 °C for 24 h. The obtained nanocomposite was cut into the desired shape and size for further use.

### **Characterizations**

Transmission Electron Microscopy was conducted on a JEOL 2100F microscope operated at 200 kV. Cross-sectional and surface morphology was carried out using a scanning electron microscope (SEM, JSM-6500F, JEOL). Crystal structure analysis was carried using the Rigaku Ultima II Powder XRD system with a Cu K $\alpha$  radiation at a scan rate of 1.5° min<sup>-1</sup> and a sampling

of  $0.02^\circ$  and analyzed using PDXL software. Fourier transform infrared spectroscopy was conducted on Thermo Scientific Nicolet iS50 FT-IR Spectrometer. X-ray photoelectron measurements were carried out using PHI Quantera XPS with 200 eV Al  $K\alpha$  X-rays. The XPS peaks were fitted using Multipak software.

Differential scanning calorimetric (DSC) analysis was performed using DSC 2920 thermal analyzer (TA Instruments, Inc.). Specimens ( $\sim 5$  mg) were scanned from 30 to  $110^\circ\text{C}$  at a heating rate of  $10^\circ\text{C}/\text{min}$ , held at that temperature for 2 min, then cooled to  $30^\circ\text{C}$  at a cooling rate of  $20^\circ\text{C}/\text{min}$  (first scan) before carrying out the second heating scan to  $350^\circ\text{C}$  at a heating rate of  $10^\circ\text{C}/\text{min}$ . Thermo-gravimetric analysis (TGA) was conducted using a TGA Q500 (TA Instruments) instrument. Specimens ( $\sim 5$  mg) were scanned from 30 to  $1000^\circ\text{C}$  at a heating rate of  $10^\circ\text{C}/\text{min}$  under a flow of nitrogen gas. The surface temperatures of the MSC samples were measured using a thermography infrared (IR) camera (FLIR A65) with a temporal resolution of 25 frames/second and a spatial resolution of  $\sim 100$  microns. The IR camera was positioned above the sample at a slightly tilted angle to allow for top illumination. Measurements were performed in air with the samples attached to a glass substrate. Optical illumination from a 532-nm continuous wave (CW) laser source was used to control the surface temperature of the samples. The illumination power was adjusted to 20 mW and 40 mW to establish a nominal surface temperature of  $105^\circ\text{C}$  for the unmodified and modified MSC, respectively. Static uniaxial tensile properties of the MSCs were determined with a dynamic mechanical analyzer (DMA Q800, TA Instrument). Rectangular sheets of a width of 5 mm and a length of 15 mm were tested in controlled force mode with a 0.5 N/min force ramp until the fracture occurred.

### **Electrochemical Characterization**

For room-temperature electrochemical studies, cells were made in a CR2032 coin cell purchased from MTI with 6M KOH as the electrolyte. For high-temperature studies, CR2032 components (Hohsen Corp.) were used with EMITFSI as the electrolyte. Cyclic Voltammetry and Impedance studies were carried out using AUTOLAB PGSTAT 302 N ECOCHEMIE. Charge-discharge studies were performed using a battery test station from Arbin Instruments.

### CONFLICTS OF INTERESTS

The authors declare no conflicts of interests.

### ELECTRONIC SUPPLEMENTARY INFORMATION

The Supplementary Information (SI) can be found online.

### AUTHOR CONTRIBUTIONS

M.M.R. and P.M.A. designed and coordinated the study, F.Y. and D.S. fabricated MSCs, D.S., A.B., S.H, A.B.P. characterized electrochemical performance of MSCs, M.A.S.R, D.S., F.C.R., H.R., S.R. characterized structural, thermal, and mechanical studies, M.M.R., P.M.A, N.A.K., D.S. cowrote the paper. M.M.R., P.M.A., and N.A.K. discussed the results and commented on the manuscript.

### ACKNOWLEDGEMENT

All authors would like to thank Shared Equipment Authority at Rice University for their support. N.A.K is grateful for Vannewar Bush DoD Fellowship to N.A.K. titled "Engineered Chiral Ceramics" ONR N000141812876 and NSF project "Energy- and Cost-Efficient Manufacturing Employing Nanoparticles", NSF 1463474.

### REFERENCES

- 1 Q. Li, F.-Z. Yao, Y. Liu, G. Zhang, H. Wang and Q. Wang, *Annu. Rev. Mater. Res.*, 2018, **48**, 219–243.
- 2 R. S. Borges, A. L. M. Reddy, M. T. F. Rodrigues, H. Gullapalli, K. Balakrishnan, G. G. Silva and P. M. Ajayan, *Sci. Rep.*, , DOI:10.1038/srep02572.
- 3 J. Jiang, *J. Electrochem. Soc.*, 2017, **164**, H5043–H5048.
- 4 Q. Li, L. Chen, M. R. Gadinski, S. Zhang, G. Zhang, H. Li, A. Haque, L. Q. Chen, T. Jackson and Q. Wang, *Nature*, 2015, **523**, 576–579.
- 5 M. Wang, A. Emre, S. Tung, A. Gerber, D. Wang, Y. Huang, V. Cecen and N. A. Kotov, *ACS Nano*, 2019, **13**, 1107–1115.
- 6 M. Yanilmaz, M. Dirican, A. M. Asiri and X. Zhang, *J. Energy Storage*, , DOI:10.1016/j.est.2019.100766.
- 7 H. Peng, Y. Lv, G. Wei, J. Zhou, X. Gao, K. Sun, G. Ma and Z. Lei, *J. Power Sources*,

- 2019, **431**, 210–219.
- 8 M. Yang, K. Cao, L. Sui, Y. Qi, J. Zhu, A. Waas, E. M. Arruda, J. Kieffer, M. D. Thouless and N. A. Kotov, *ACS Nano*, 2011, **5**, 6945–6954.
- 9 M. Q. Jian, H. H. Xie, K. L. Xia and Y. Y. Zhang, in *Industrial Applications of Carbon Nanotubes*, Elsevier Inc., 2017, pp. 433–476.
- 10 S. R. Kwon, J. Harris, T. Zhou, D. Loufakis, J. G. Boyd and J. L. Lutkenhaus, *ACS Nano*, 2017, **11**, 6682–6690.
- 11 S. Bose, S. Basu, A. Das, M. Rahman and L. T. Drzal, *J. Appl. Polym. Sci.*, , DOI:10.1002/app.45099.
- 12 C. Meng, C. Liu, L. Chen, C. Hu and S. Fan, *Nano Lett.*, 2010, **10**, 4025–4031.
- 13 J. Zhu, W. Cao, M. Yue, Y. Hou, J. Han and M. Yang, *ACS Nano*, 2015, **9**, 2489–2501.
- 14 S. R. Kwon, M. B. Elinski, J. D. Batteas and J. L. Lutkenhaus, *ACS Appl. Mater. Interfaces*, 2017, **9**, 17125–17135.
- 15 C. Chen, D. Liu, L. He, J. M. Razal, A. Nicholas, C. Chen, D. Liu, L. He, S. Qin, J. Wang, J. M. Razal and N. A. Kotov, 2019, 247–261.
- 16 M. M. Rahman, A. B. Puthirath, A. Adumbukulath, T. Tsafack, H. Robotjazi, M. Barnes, Z. Wang, S. Kommandur, S. Susarla, S. M. Sajadi, D. Salpekar, F. Yuan, G. Babu, K. Nomoto, S. M. Islam, R. Verduzco, S. K. Yee, H. G. Xing and P. M. Ajayan, *Adv. Funct. Mater.*, , DOI:10.1002/adfm.201900056.
- 17 K. Sharma, A. Arora and S. K. Tripathi, 2019, **21**, 801–825.
- 18 C. S. Li, M. S. Zhan, X. C. Huang and H. Zhou, *J. Appl. Polym. Sci.*, 2012, **126**, 552–558.
- 19 N. O. Weiss, H. Zhou, L. Liao, Y. Liu, S. Jiang, Y. Huang and X. Duan, *Adv. Mater.*, 2012, **24**, 5782–5825.
- 20 F. Barthelat, Z. Yin and M. J. Buehler, *Nat. Rev. Mater.*, , DOI:10.1038/natrevmats.2016.7.
- 21 U. G. K. Wegst, H. Bai, E. Saiz, A. P. Tomsia and R. O. Ritchie, *Nat. Mater.*, 2015, **14**, 23–36.
- 22 G. Xiao, J. Di, H. Li and J. Wang, *Compos. Sci. Technol.*, 2020, **189**, 108021.
- 23 J. Fan, Z. Shi, L. Zhang, J. Wang and J. Yin, 2012, 7046–7055.
- 24 G. R. Bhimanapati, D. Kozuch and J. A. Robinson, *Nanoscale*, 2014, **6**, 11671–11675.
- 25 H. H. Huang, K. K. H. De Silva, G. R. A. Kumara and M. Yoshimura, *Sci. Rep.*, 2018, **8**, 2–10.
- 26 C. Arrieta, E. David, P. Dolez and T. Vu-Khanh, *Polym. Compos.*, 2011, **32**, 362–367.
- 27 M. Mukherjee, S. Kumar, S. Bose, C. K. Das and A. P. Kharitonov, *Polym. - Plast. Technol. Eng.*, 2008, **47**, 623–629.
- 28 S. Radhakrishnan, D. Das, A. Samanta, C. A. De Los Reyes, L. Deng, L. B. Alemany, T. K. Weldeghiorghis, V. N. Khabashesku, V. Kochat, Z. Jin, P. M. Sudeep, A. A. Martí, C. W. Chu, A. Roy, C. S. Tiwary, A. K. Singh and P. M. Ajayan, *Sci. Adv.*, 2017, **3**, 1–9.
- 29 S. Vinod, C. S. Tiwary, P. A. Da Silva Autreto, J. Taha-Tijerina, S. Ozden, A. C. Chipara, R. Vajtai, D. S. Galvao, T. N. Narayanan and P. M. Ajayan, *Nat. Commun.*, 2014, **5**, 1–9.
- 30 J. Fan, Z. Shi, M. Tian and J. Yin, *RSC Adv.*, 2013, **3**, 17664–17667.
- 31 B. Gupta, N. Kumar, K. Panda, V. Kanan, S. Joshi and I. Visoly-Fisher, *Sci. Rep.*, 2017, **7**, 1–14.
- 32 S. J. Kerber, J. J. Bruckner, K. Wozniak, S. Seal, S. Hardcastle and T. L. Barr, *J. Vac. Sci. Technol. A Vacuum, Surfaces, Film.*, 1996, **14**, 1314–1320.
- 33 J. Fan, Z. Shi, L. Zhang, J. Wang and J. Yin, *Nanoscale*, 2012, **4**, 7046–7055.
- 34 Y. Li, G. Ren, Z. Zhang, C. Teng, Y. Wu, X. Lu, Y. Zhu and L. Jiang, *J. Mater. Chem. A*,

- 2016, **4**, 17324–17332.
- 35 L. W. Le Fevre, J. Cao, I. A. Kinloch, A. J. Forsyth and R. A. W. Dryfe, *ChemistryOpen*, 2019, **8**, 418–428.
- 36 M. D. Stoller and R. S. Ruoff, *Energy Environ. Sci.*, 2010, **3**, 1294–1301.
- 37 J. S. M. Lee, M. E. Briggs, C. C. Hu and A. I. Cooper, *Nano Energy*, 2018, **46**, 277–289.
- 38 J. Fan, Z. Shi, M. Tian and J. Yin, *RSC Adv.*, 2013, **3**, 17664–17667.
- 39 Y. Guan, W. Li, Y. Zhang, Z. Shi, J. Tan, F. Wang and Y. Wang, *Compos. Sci. Technol.*, 2017, **144**, 193–201.
- 40 T. Liu, K. Wang, Y. Chen, S. Zhao and Y. Han, *Green Energy Environ.*, 2019, **4**, 171–179.
- 41 Y. Wang, J. Velmurugan and M. V. Mirkin, *Isr. J. Chem.*, 2010, **50**, 291–305.
- 42 K. Kato, M. T. F. Rodrigues, G. Babu and P. M. Ajayan, *Electrochim. Acta*, 2019, **324**, 134871.
- 43 K. O. Oyedotun, T. M. Masikhwa, S. Lindberg, A. Matic, P. Johansson and N. Manyala, *Chem. Eng. J.*, 2019, **375**, 121906.